APPLIED ECOLOGY

Radioisotopic chronology of Ocean Anoxic Event 1a: Framework for analysis of driving mechanisms

Youjuan Li[1]†, Brad S. Singer[1]*, Reishi Takashima[2], Mark D. Schmitz[3], Luca G. Podrecca[4], Bradley B. Sageman[4], David Selby[5], Toshiro Yamanaka[6], Michael T. Mohr[3], Keiichi Hayashi[7], Taiga Tomaru[8], Katarina Savatic[4]

The timing, tempo, and causative mechanisms of Ocean Anoxic Event 1a (OAE1a), one of several such abrupt perturbations of the Mesozoic global carbon cycle, remain uncertain. Mudstones interbedded with tuffs in Hokkaido, Japan preserve carbon and osmium isotope shifts recording OAE1a. U-Pb zircon ages of tuffs constrain the OAE1a onset to 119.55 +0.072/−0.079 million years ago (Ma) and its duration to 1116 +87/−93 thousand years (kyr). Isotopic excursions of osmium followed by carbon that mark the rapid onset of OAE1a each lasted ~115 kyr. Critically, the occurrence of index fossil *Leupoldina cabri* in the Hokkaido OAE1a section, which also caps and thus postdate Ontong Java Plateau (OJP) basalts, has a U-Pb zircon age of ~118.7 to 118.4 Ma. Therefore, OJP volcanism remains a probable source of unradiogenic osmium and light carbon and a causative mechanism of OAE1a.

INTRODUCTION

Ocean Anoxic Event 1a (OAE1a) is characterized by worldwide deposition of organic-rich sediments, biotic crises, accelerated evolution of marine organisms, and abrupt carbon isotope anomalies in marine and continental carbonate and organic matter, reflecting one of the largest perturbations of the global carbon cycle and climate system of the past 200 million years (*1*–*6*). The event is associated with changes in global temperature, ocean acidification, increased continental weathering, accelerated hydrological cycling, enhanced nutrient discharge to the oceanic reservoir, and an increase in organic productivity (*7*–*12*). The OAE1a was first identified (*1*, *2*) and correlated with a distinctive black shale, the Livello Selli in the Umbro-Marchean Appenines, Italy (*13*); globally, it can be identified by a negative and then positive carbon isotope ($\delta^{13}C$) excursion (*3*, *14*) as well as a marked shift to relatively unradiogenic osmium isotope composition (Os_i) preserved in organic matter (*7*, *15*). The $\delta^{13}C_{carb}$ and $\delta^{13}C_{org}$ records of OAE1a have been developed into a chemostratigraphic segmentation, with initiation marked by a negative $\delta^{13}C$ shift (base of C isotope segment C3) that is associated with the onset of black shale facies in many sites. The termination of black shale deposition, interpreted as the end of OAE1a (*1*, *6*), occurs at the top of segment C6, about midway through the positive excursion (*3*).

OAEs were originally conceived as global perturbations in Earth's carbon cycle associated with widespread but not total anoxia because some marine areas will always be better ventilated and thus lack black shale development (*6*). Although the extent of organic-rich facies cannot uniquely provide an accurate marker of OAE duration (*3*, *6*), an interpretation of the termination of OAE1a based on this concept has become the standard within the OAE1a literature [e.g., (*7*–*11*)]. Alternatively, the end of the positive $\delta^{13}C$ excursion (defined as a return to "background" values, e.g., the top of segment C7) provides a different definition of OAE1a termination, like that which is applied to OAE2 (*6*). Herein, we present a chemostratigraphic framework anchored with radioisotopic dates that can constrain either definition with limits that incorporate both stratigraphic and age uncertainties.

Competing volcanic mechanisms that may have triggered OAE1a vary in nature, process, and probability, and process-driven linkages between changes in climate, oceanic fertility, marine chemistry, and biotic response have been the subject of ongoing debate (*5*, *7*, *10*, *15*–*22*). Understanding proposed process linkages can only be as robust as our confidence in their rates and patterns of change, necessitating precise and accurate chronology for the geochemical signals defining OAE1a as well as those of its proposed volcanic sources (*5*, *23*). Hitherto, the timing of OAE1a has been ambiguous, reflecting uncertainties in dating methods (*7*, *23*–*28*). The duration of OAE1a has been estimated using astrochronologic methods (*23*–*25*, *27*, *29*), but these age models are not anchored by radioisotopic dating due to the absence of volcanic ash beds in most OAE1a sections (*6*, *30*, *31*). The Yezo Group, Hokkaido, Japan (Fig. 1 and fig. S1) presents a superb opportunity to address this problem because it is a continuous sequence of Aptian to Paleocene hemipelagic sediment in a mid-latitude Pacific Ocean–facing forearc basin comprising pre-, syn-, and post-OAE1a deposits interbedded with hundreds of rhyolitic tuffs (Fig. 1, A and B) (*30*, *32*).

The Soashibetsu-gawa Formation comprises ~450 to 700 m of siliceous dark gray mudstone intercalated with rhyolitic tuffs that are 10 to 30 cm thick, with some ~1 to 7 m thick (Fig. 1C and figs. S1 and S2). We define the 0.0-m level in the middle of this formation (Fig. 1C). *Leupoldina cabri* foraminifera, a biostratigraphic index for the core of OAE1a (*3*), have been documented previously in the Soashibetsu-gawa Formation (*33*, *34*) and provide a marker for correlation between the two sections we have sampled (Fig. 1C and fig. S3). The onset of OAE1a is expressed as a prominent negative $\delta^{13}C_{org}$

[1]Department of Geoscience, University of Wisconsin-Madison, Madison, WI 53706, USA. [2]Tohoku University Museum, Tohoku University, Aoba-ku, Sendai 980-8578, Japan. [3]Department of Geosciences, Boise State University, Boise, ID 83725, USA. [4]Department of Earth and Planetary Sciences, Northwestern University, Evanston, IL 60208, USA. [5]Department of Earth Science, Durham University, Durham DH1 3LE, UK. [6]School of Marine Resources and Environment, Tokyo University of Marine Science and Technology, Tokyo 108-8477, Japan. [7]Geological Survey of Hokkaido, Environmental and Geological Research Department, Hokkaido Research Organization, Nishi-12, Kita-19, Kita-ku, Sapporo, Hokkaido 060-0819, Japan. [8]Department of Earth Science, Graduate School of Science, Tohoku University, Aoba-ku, Sendai 980-8578, Japan.
*Corresponding author. Email: bsinger@wisc.edu
†Present address: Institute of Geology and Geophysics, Chinese Academy of Sciences, Beijing 100029, China.

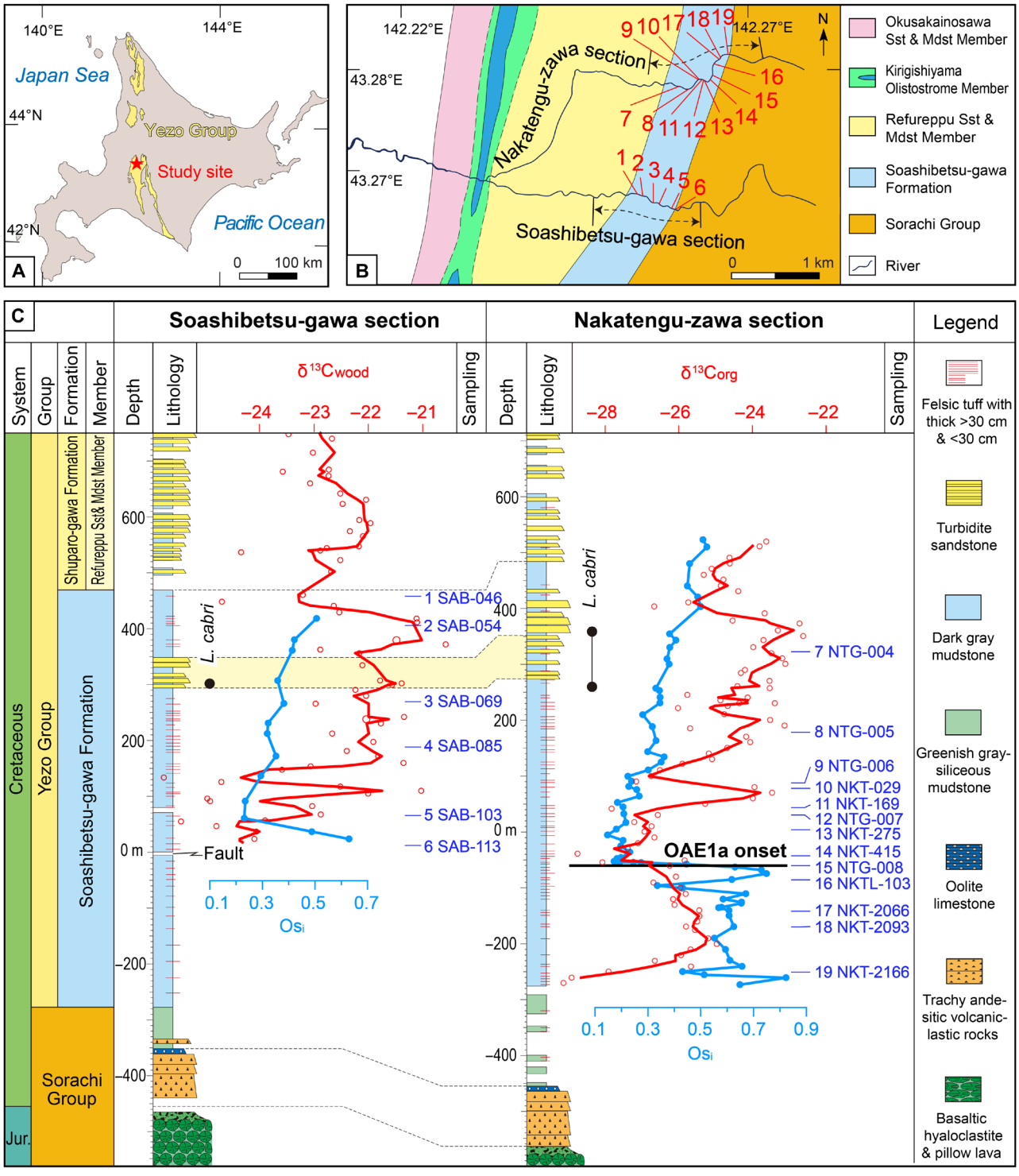

Fig. 1. Location and chemostratigraphy of SAB and NKT sections, Hokkaido, Japan. (**A**) Location of sections and samples. (**B**) Red numbers along parallel sections through vertically dipping strata that is younger to the west correspond to dated tuffs in Table 1. (**C**) Lithography and chemostratigraphy (data S2 and S3); red open circles represent individual $\delta^{13}C$ measurements; red lines show the upsection moving average (data S2). Jur., Jurassic; Os_i, initial $^{187}Os/^{188}Os$ at 119 Ma. Numbered blue labels show positions of dated tuff samples.

excursion associated with a distinctive shift in Os_i toward unradiogenic values (*7*, *15*); this is followed by a positive $\delta^{13}C_{org}$ excursion spanning >400 m of overlying strata (Fig. 1C) (*30*, *32*). Herein, we present carbon and osmium isotope compositions from mudstones in Soashibetsu-gawa (SAB) and the better documented Nakatengu-zawa (NKT) canyons, together with chemical abrasion–isotope dilution–thermal ionization mass spectrometry (CA-ID-TIMS) U-Pb zircon dates for 19 tuff samples (Fig. 1C). We integrate this chemostratigraphy and geochronology within a Bayesian age model to probabilistically determine the onset, termination, and duration of OAE1a.

RESULTS

Biostratigraphy and chemostratigraphy

Foraminifera, specifically the index fossil *L. cabri*, and radiolaria confirm an Early Aptian age for the Soashibetsu-gawa Formation (fig. S3) (*3*, *6*, *30*, *34*, *35*). Recognition of the OAE1a interval within the Soashibetsu-gawa Formation and correlation to the global $\delta^{13}C$ segmentation scheme of OAE1a (*3*, *4*) are aided by the presence of *L. cabri* in fine-grained mudstone. Moreover, the acme of genus *Leupoldina* aligns with the *L. cabri* biozone and OAE1a interval (*36*). First Appearance Datums (FADs) for *L. cabri* vary from within the Globigerinelloides blowi biozone (*37*, *38*) to the top of this zone (*6*), where it is associated with the most negative $\delta^{13}C$ values of isotope segment C3 (*39*); this variation in FADs is reflected in the dashed boundary between the *G. blowi* and *L. cabri* biozones in many publications. The Last Appearance Datum for *L. cabri* occurs just following the most $\delta^{13}C$-enriched values of isotope segment C7 (see below) and defines the end of the *L. cabri* biozone (*6*, *39*). As such, *L. cabri* is a relatively robust marker for the OAE1a interval. Stratigraphic levels in the SAB and NKT sections that include *L. cabri* specimens are shown in Fig. 1.

In the NKT section, $\delta^{13}C_{org}$ values from bulk mudstone are generally consistent with similar bulk measurements from global pelagic and European hemipelagic OAE1a records (*3*, *6*, *9*). These values are, however, depleted by at least 2 to 3 per mil (‰) relative to isolated woody fragments (terrigenous carbon) analyzed from the SAB and NKT sections in previous works (*30*, *40*) as well as this study (Fig. 1C). This is consistent with the conclusion that the bulk mudstone $\delta^{13}C_{org}$ signal in the NKT section reflects a mixture of marine and terrestrial organic matter sources that record the character of the globally recognized OAE1a profile and segmentation scheme (*3*, *6*). The sedimentary organic matter in the Yezo Group is mainly composed of detrital woody materials (opaque and translucent phytoclasts) and a small amount (<5.2%) of cuticles, spore/pollen grains, and dinoflagellate cysts (*40*). Chemostratigraphic correlation of the $\delta^{13}C$ profile (fig. S4) is supported by Os_i stratigraphy [e.g., (*7*, *15*)]. Both chemostratigraphic profiles are shown with the C isotope segmentation scheme in Figs. 1 and 2 (expanded methodology is in the Supplementary Materials).

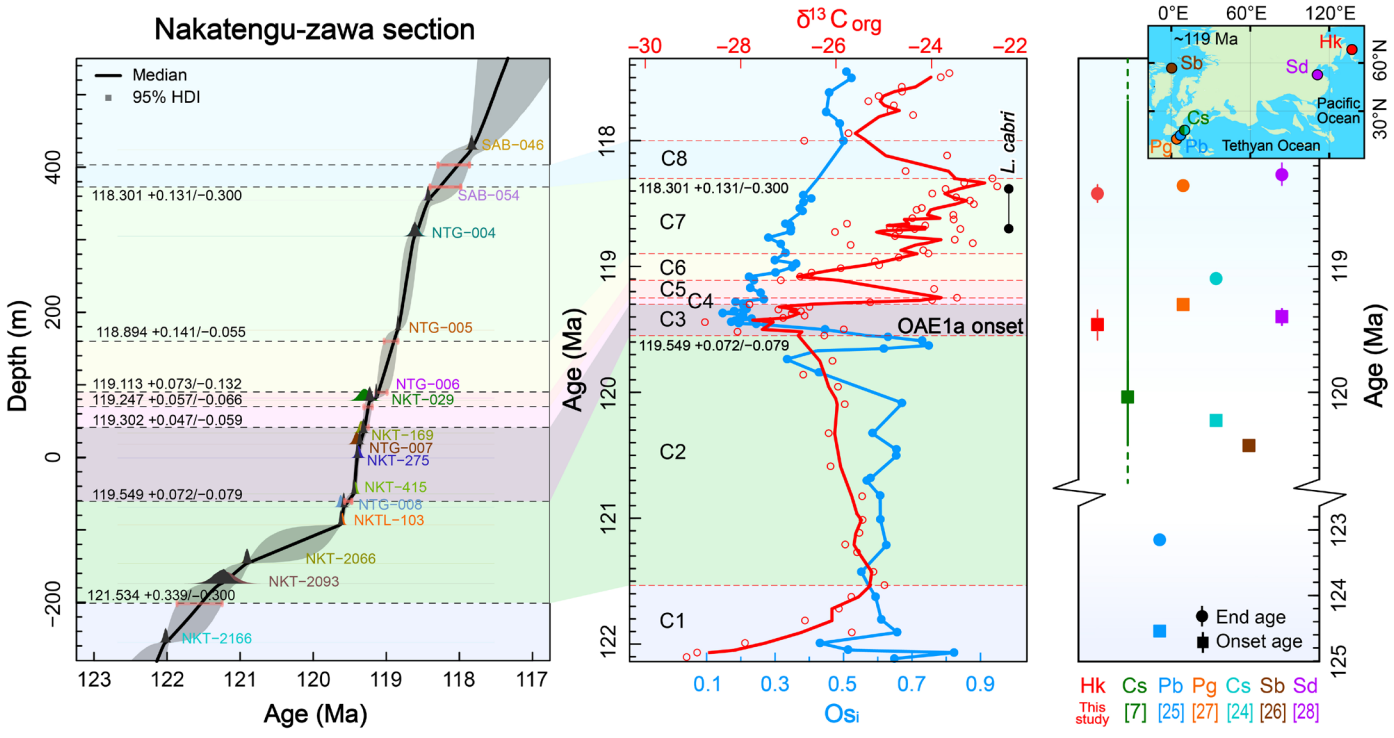

Fig. 2. Composite age model constructed from the NKT section and comparison to other estimates for the age and duration of OAE1a. Two youngest dated tuffs SAB-046 and SAB-054 correlated from the nearby SAB section. Shaded distributions in color denote the summed probability distribution of $^{206}Pb/^{238}U$ dates for each tuff, as likelihood inputs into Bayesian modeling. Posterior distributions are superimposed in black on original likelihoods. The black solid line indicates the median, and the 95% HDI indicated by light gray shading represents the model uncertainty for all interpolated points between tuffs. The right panel illustrates estimates for the age of onset and termination of OAE1a at other sites compared to our results from Hokkaido. Note that, as described in the text, OAE1a is not consistently defined. Hk, Hokkaido; Cs, Cismon; Pb, Piobbico; Pg, Poggio le Guaine; Sb, Svalbard; Sd, Shandong. Only symbols with an error bar represent dates with an uncertainty value; otherwise, no uncertainty is provided.

A key underlying assumption of $\delta^{13}C$ chemostratigraphic correlation is that the isotopic mass balance of the global carbon cycle may be consistently expressed throughout surface Earth environments and, similarly (although not identically), in both organic and carbonate materials. Although differences in local sedimentation rate histories and basinal biogeochemical conditions (productivity and anoxia) can alter the local character of preserved isotopic records, it is possible to establish criteria for effective correlation, such as recognition of similarities in negative and positive shifts as well as overall minima and maxima in the signal. Combining independent chemostratigraphic profiles, such as $\delta^{13}C$ and Os_i, and identifying biostratigraphic constraints strengthen correlation efforts.

The previously published $\delta^{13}C_{wood}$ record from the SAB section (*30*, *40*), like our $\delta^{13}C_{wood}$ record from SAB, preserves the major features of the global $\delta^{13}C$ profile spanning OAE1a (see below), but sampling was not at high resolution, especially given the extreme sedimentation rates and thickness of these deposits. These features of the global $\delta^{13}C$ profile are also evident in the NKT bulk mudstone record, but with higher sample density, the profile is more variable. This is not unexpected given the depositional system (continental slope mudstones with common turbidites), potential influences on terrestrial organic matter pools, and variations in the delivery of terrestrial material to the site of deposition. Confidence in our identification of the chemostratigraphic segmentation presented in Figs. 1 and 2 is based on specific attributes of the $\delta^{13}C$ records that follow the original C segment scheme (*3*) as well as its more recent incarnations (*6*, *41*), the identification of appropriate biostratigraphic indices as described above, and the similarity of the Os_i record to other such profiles in widely distributed OAE1a sites [e.g., (*7*, *15*, *21*, *42*)]. For presentation purposes, Figs. 1 and 2 show a moving average $\delta^{13}C_{org}$ profile; details of our chemostratigraphic analysis (including estimation of uncertainties associated with C segment definitions) are presented in the Supplementary Materials.

Initiation of OAE1a is defined at the base of segment C3 (*3*, *6*); this interval is uniquely defined in all published OAE1a chemostratigraphic records by the most depleted $\delta^{13}C$ values associated with the event, dropping as low as −4‰ in $\delta^{13}C_{carb}$ (*6*) and −28‰ in $\delta^{13}C_{org}$ [(*41*) and this study]. A portion of the negative shift that precedes the most depleted values from a pre-event background that is generally more positive ($\delta^{13}C_{carb} > 2$‰ and $\delta^{13}C_{org} > -24$‰) is typically included in C3, and in several records (e.g., Cismon, Italy; Cau, Spain), the boundary between C2 and C3 is placed at a sharp inflection to more negative values within this trend (*6*). The global Os_i record further distinguishes the C2 to C3 interval (*7*, *15*, *21*, *42*): There is a distinctive oscillation to unradiogenic and then radiogenic Os_i compositions in the upper part of C2, followed by the main shift to unradiogenic values (>0.13 to <0.2) that occurs in association with segment C3. Although the Os_i record generally assists in the correlation of OAE1a onset due to the pronounced shift to unradiogenic values, there are variations in Os_i profiles. For example, the interval we define as C3 in the NKT record based on the most negative $\delta^{13}C$ values has the pronounced shift to unradiogenic Os_i at its base (Figs. 1 and 2 and fig. S4), whereas this shift occurs within the C3 segment in many Tethyan sites (*7*). One possible explanation for this difference is that the $\delta^{13}C$ signal is delayed relative to the global record because it is mainly carried in terrestrial organic matter being transported downslope. However, a recently published Os_i record from Deep Sea Drilling Project (DSDP) Site 463, which is also from the Pacific region, shows the same alignment of the Os_i shift with the onset of negative $\delta^{13}C$ values and the base of segment C3 (*42*). Thus, a second possibility is that the Os_i signal, sourced from Ontong Java Plateau (OJP) volcanism, was recorded earlier in the Pacific region (and concurrent with the $\delta^{13}C$ shift) compared to other sites. Similarity of the NKT record to Site 463 and the fact that Os_i signals are only transmitted via advection of oceanic water masses, whereas carbon signals cycle through the atmosphere, support this interpretation. On the basis of the Bayesian age model, the temporal lag between the turning point in $\delta^{13}C$ marking the base of segment C3 and the shift in Os_i in Tethyan sections is ~39 thousand years (kyr), well within the uncertainty of the radioisotopic dates. The Os_i values remain low for the duration of the C3 segment in both the NKT section (Figs. 1 and 2 and fig. S4) and Site 463 (*42*) with the subsequent shift toward more positive values interpreted to represent segment C4.

The most positive $\delta^{13}C$ values associated with the *L. cabri* biozone and OAE1a occur within the upper part of segment C7 and may exceed 4 to 5‰ for $\delta^{13}C_{carb}$ (*6*) and −23‰ for $\delta^{13}C_{org}$ [(*41*) and this study]. Segment C7 is commonly identified as a plateau (which may be relatively stable, or variable) of the most positive $\delta^{13}C$ values that follows the C6 positive shift and terminates where values very clearly start trending more negative, defining segment C8. In records that include data extending above the positive $\delta^{13}C$ excursion [e.g., (*42*)], Os_i compositions recover to at least 0.5 within the declining trend of $\delta^{13}C$ values that define C8. In the NKT section, Os_i values also recover to 0.5 in association with the declining $\delta^{13}C$ values that we interpret to define segment C8 (Figs. 1 and 2 and fig. S4).

In many published records, the interval between C3 and C7 includes two prominent positive shifts that ramp up to the enriched $\delta^{13}C$ values of the C7 plateau, with a relatively stable plateau or variable interval between them (segment C5). In this scenario, segments C4 and C6 are the distinctive positive shifts. However, there is substantial variation within this interval among OAE1a sites globally and segment C5 may manifest as a plateau, an interval of declining values, or an interval with marked variation (*6*). In some cases, authors do not identify individual segments between C3 and C7 due to this variability yet still feel confident in their overall recognition of the OAE1a event based on the integration of $\delta^{13}C$ observations, other chemostratigraphic indicators, for example, Os_i, and biostratigraphy. The SAB and NKT records are similar in that the character of the C4, C5, and C6 segments are variable, with C4 showing a much larger positive shift than is typical, followed by a similarly large negative trend in C5 [not unlike ODP Site 866, also in the Pacific (*43*)]. The C6 positive shift in the NKT record, however, is similar to many other sites. Thus, although there is clearly some uncertainty in the assignment of C segments C4 and C5, as in many OAE1a chemostratigraphic records, relative confidence in the definitions of the C3 and C7 segments is high.

U-Pb zircon chronology

Zircon crystals from 19 tuff samples were dated using U-Pb CA-ID-TIMS (methods and uncertainties in Supplementary Text, data S1, and figs. S5 and S6). There are multiple approaches to interpreting the dispersed sets of U-Pb dates acquired from each tuff (fig. S5) to determine an eruption age. The weighted mean zircon ages in Table 1 are based on the youngest set of concordant $^{206}Pb/^{238}U$ dates that meet the modified Thompson Tau outlier rejection criteria [$P = 0.05$ (*44*)] and yield acceptable mean square weighted deviations [e.g., (*45*, *46*)]. These ages are mutually resolvable outside uncertainty,

Table 1. Summary of single zircon $^{206}Pb/^{238}U$ CA-ID-TIMS results from tuffs in Hokkaido, Japan. *N*, number of single crystal zircon dates used for age calculation relative to the total number of dates; ±95% conf.$_{anal}$, analytical uncertainty only at the 95% confidence interval; ±95% conf.$_{tr}$, analytical plus tracer uncertainty; ±95% conf.$_{tot}$, fully propagated uncertainty at the 95% confidence interval including analytical, tracer, and decay constant uncertainties; MSWD, mean square weighted deviation; Wtd. mean age, weighted mean age.

Tuff number	Tuff sample ID	Height a bove base of section (m)	Latitude (°N)	Longitude (°E)	*N*	MSWD	Wtd. mean age (Ma)	±95% conf.$_{anal}$	±95% conf.$_{tr}$	±95% conf.$_{tot}$
SAB section										
1	SAB-046	454.5	43.267130	142.254067	5 of 12	0.70	117.830	0.061	0.070	0.145
2	SAB-054	403.3	43.267080	142.254800	11 of 21	1.81	118.439	0.043	0.056	0.140
3	SAB-069	263.7	43.266230	142.256350	4 of 6	0.11	118.880	0.098	0.104	0.165
4	SAB-085	183.5	43.266170	142.257200	5 of 10	0.19	118.853	0.052	0.063	0.143
5	SAB-103	60.7	43.265630	142.258967	7 of 7	0.29	119.253	0.055	0.066	0.145
6	SAB-113	13.0	43.265530	142.259550	6 of 10	0.60	121.282	0.164	0.168	0.213
NKT section										
7	NTG-004	305.0	43.278500	142.260117	3 of 12	0.01	118.597	0.134	0.139	0.189
8	NTG-005	176.0	43.278400	142.261617	6 of 11	1.75	118.840	0.030	0.046	0.136
9	NTG-006	82.5	43.279033	142.262783	7 of 9	1.83	119.139	0.024	0.043	0.136
10	NKT-029	78.4	43.279117	142.262933	3 of 5	0.14	119.298	0.145	0.149	0.197
11	NKT-169	34.2	43.279250	142.263400	9 of 10	0.73	119.344	0.063	0.073	0.147
12	NTG-007	18.7	43.279483	142.263617	3 of 3	0.77	119.406	0.076	0.084	0.154
13	NKT-275	0.0	43.279183	142.263717	6 of 6	2.21	119.382	0.061	0.070	0.147
14	NKT-415	−49.5	43.279153	142.264572	5 of 9	2.09	119.419	0.040	0.053	0.140
15	NTG-008	−67.8	43.279733	142.264833	7 of 9	0.64	119.630	0.057	0.067	0.145
16	NKTL-103	−92.1	43.280700	142.265075	6 of 7	2.29	119.616	0.044	0.057	0.141
17	NKT-2066	−145.0	43.281344	142.265833	3 of 6	0.87	120.907	0.060	0.070	0.147
18	NKT-2093	−173.0	43.281805	142.266111	5 of 6	0.82	121.201	0.318	0.320	0.346
19	NKT-2166	−254.0	43.282003	142.267218	4 of 17	1.61	122.020	0.054	0.065	0.147

obey stratigraphic order, and are thus regarded as reliable depositional timing estimates for the corresponding strata. These age likelihoods and stratigraphic positions are integrated using a Bayesian age-depth modeling approach (Fig. 2). Figure S7 compares our preferred weighted mean ages to those derived using a Bayesian eruption age algorithm (*45*). The two age interpretation methods agree within uncertainties on all accounts and, when integrated into the Bayesian age-depth model, do not yield differences in stratigraphic interval durations that would alter our geologic interpretations (fig. S7).

DISCUSSION

An OAE1a age model

Our U-Pb age determinations provide an age model for the $\delta^{13}C$ and Os_i shifts associated with OAE1a recorded in the NKT section (Fig. 2). All ages are consistent with stratigraphic superposition within analytical uncertainties (Figs. 1 and 2 and Table 1) and are considered robust estimates for the time since deposition of corresponding strata. The composite chronostratigraphy and Bayesian age model (*47*) developed from the NKT section is supported by correlation of dated tuff horizons from both the SAB and NKT sections (Fig. 2). Using this age model, which reveals a remarkably constant and high rate of deposition at 39 cm/kyr, the timing of carbon isotope segments of OAE1a can be probabilistically determined from the posterior age distribution at the specific stratigraphic position.

Although age estimates can be derived for any part of the $\delta^{13}C$ and Os_i profiles using our timescale, we focus on those for the base of $\delta^{13}C$ segment C3 and the base and top of segment C7. The abrupt negative $\delta^{13}C_{org}$ and unradiogenic Os_i excursions that we interpret to define the base of segment C3 at −60.7 m in the NKT section occur at 119.549 +0.072/−0.079 million years ago (Ma) (Fig. 2 and table S1). The top of segment C6 at +160.3 m in the NKT succession occurs at 118.894 +0.141/−0.055 Ma. The top of segment C7 at +372.8 m in the NKT section corresponds to a Bayesian age of 118.301 +0.131/−0.300 Ma; however, we note that tuff SAB-054 correlates to within 19 m of the top of the C7 segment and has an age uncertainty of ±0.043 Ma (Table 1). The Bayesian age model likely exaggerates the true uncertainty for this boundary, which we suggest is about ±0.043 Ma. Using these ages, we estimate a mean duration of OAE1a from base C3 to top C7 of 1116 +87/−93 kyr (ranging from 1203 to 1023 kyr), and from base C3 to top C6, it is 647 +103/−154 kyr (ranging from 750 to 493 kyr).

Our U-Pb ages overlap the only other radioisotopic age determination for OAE1a, a Re-Os errorchron of 120.0 ± 3.4 Ma from black shale in the Cismon core, Italy (Fig. 2) (*7*). Cyclostratigraphy of the Piobbico core, Italy suggests the onset and termination of OAE1a at 124.55 and 123.16 Ma, respectively, but defines the termination at the top of C6 and assumes an age of 99.6 Ma for the

Albian-Cenomanian boundary (Fig. 2) (*25*). Astronomical tuning of the Poggio le Guaine core, Italy (*27*) is anchored to an Aptian-Albian boundary age of 113.0 Ma. The base and top of the Selli level in the astronomical age model developed for the Cismon APTICORE assume an age of 121 Ma for the base of magnetic polarity Chron M0r (Fig. 2) (*24*). From magnetostratigraphy of cores in Svalbard, Norway, an age of 120.4 Ma for the base of OAE1a is interpolated assuming an age of 121.2 ± 0.4 Ma for the base of magnetic polarity Chron M0r (Fig. 2) (*26*, *48*, *49*). Alternatively, the onset of OAE1a was proposed to occur at 119.40 ± 0.12 Ma based on an integrated $^{40}Ar/^{39}Ar$ and U-Pb radioisotopic age of 120.29 ± 0.09 Ma for the base of Chron M0r in Jiaolai Basin, China (Fig. 2) (*28*). Moreover, the age estimates from Norway and China are extrapolations using the Cismon APTICORE astrochronologic age model for OAE1a (*24*). In contrast to these estimates, our radioisotopic ages offer an important step forward in understanding the timing of OAE1a, regardless of preferred definition of the event, and they are ~1 Ma younger than in current timescales (*48*, *49*).

Astrochronologic age models, using the Livello Selli (black shale–based) definition of OAE1a, yield durations of (i) ~1000 to 1300 kyr for the Cismon, Santa Rosa Canyon, and DSDP Site 398 sections (*23*); (ii) 1110 ± 110 kyr from the Cismon APTICORE (*24*); (iii) ~1400 thousand years ago from Piobbico core (*25*); (iv) 1157 kyr from the La Bédoulian succession, France (*29*); and (v) ~920 kyr from the Poggio le Guaine core (*27*). Our radioisotopic estimate of 1116 +87/−93 kyr for the duration in the NKT section is thus remarkably similar to the average of prior estimates of OAE1a duration from astrochronology. Bayesian inversion of the Cismon APTICORE record yields the only age model with a quantifiable uncertainty (*24*), with a duration of OAE1a that is indistinguishable from our estimate of 1116 +87/−93 kyr. However, the durations of OAE1a from the Cismon APTICORE (*24*), and other astronomically dated records discussed above, define the interval from base C3 to top C6 and thus do not include segment C7. Incorporation of improved age control from our radioisotopic dating framework will help to anchor astrochronologies and lead to convergence among these different approaches to the OAE1a temporal framework.

Correlation to other OAE1a records

Although the pattern and absolute magnitude of the C isotope excursions that define OAE1a vary from site to site due to differences in organic matter source, degree of bottom water anoxia, rates and types of primary productivity, and/or history of sedimentation and stratal preservation (Fig. 3) (*50*), the general character and timing of these excursions appear to be preserved in both $\delta^{13}C_{org}$ and $\delta^{13}C_{carb}$ records of marine and terrestrial deposits (*51*). Like others (*6*, *51*), we interpret the $\delta^{13}C$ peaks and troughs that define carbon isotope segments to reflect globally synchronous shifts in the isotope mass balance of the surface carbon reservoir (*23*). Thus, carbon isotope chemostratigraphy provides a powerful tool for the global correlation of OAE1a. The $\delta^{13}C$ chemostratigraphy for the NKT section and chronostratigraphic framework enable the export of a precise radioisotopic age model from Japan to other OAE1a sites, including DSDP Site 463 in the Pacific Ocean, Cismon, Cau core, Chaqiela in the Tethyan Ocean, and DH-1 in the Atlantic Ocean (Fig. 3) (*6*, *20*, *31*, *52*, *53*). Our age model provides a means to quantify the timing and rates of processes that mark the onset of, and recovery from, ocean anoxia at globally distributed sites in which the proxy records vary. Moreover, the timing and sequence of carbon and osmium isotope shifts, reflecting the behavior of potential drivers of, and internal feedbacks within OAE1a can be more rigorously evaluated.

Chronology of volcanogenic drivers for OAE1a

The prominent negative carbon isotope excursion at the onset of OAE1a reflects a substantial depletion of ^{13}C in the ocean-atmosphere reservoir. The source of this light carbon is debated with possibilities including (i) volcanogenic CO_2 emissions from the Greater OJP and Kerguelen Plateau (KP) (*5*, *7*, *10*, *15*, *17*, *22*, *54*), (ii) destabilization of methane hydrates (*19*, *55*), (iii) injection of magma into organic-rich sediments in the High Arctic Large Igneous Province (HALIP) (*20*), or (iv) a combination of sources (*21*).

A volcanic CO_2 driver is supported by several geochemical and biotic changes (Fig. 4A). For instance, osmium and strontium isotope ratios shift to unradiogenic values at the onset of OAE1a, potentially indicating mantle-derived volcanic/hydrothermal activity (*39*, *56*). In more detail, the records from DSDP Site 463, Cismon, and Cau (Fig. 3) each indicate a pair of shifts in Os_i unradiogenic compositions, one prior to OAE1a and another possibly coeval with the negative carbon isotope excursion at the base of OAE1a. An enrichment in heavy trace metals in marine sediment, coeval with an increase in fertility and a decrease in nannofossil flux at the onset of OAE1a, argues in favor of a major role for submarine hydrothermal activity concentrated in the Greater OJP as the driver of anoxia (*5*).

Simulations using proxy records of atmospheric PCO_2 (partial pressure of CO_2) and $\delta^{13}C$ within the sedimentary succession at Cau, Spain support both methane emission and volcanic CO_2 as triggers for the negative carbon isotope excursion at the onset of OAE1a (*21*). This model suggests that carbon was first released from an extremely ^{13}C-depleted reservoir, such as thermogenic methane via sill intrusion into marine organic-rich sediments within the HALIP or destabilization of methane hydrates (*19*, *20*). Following this initial phase, less ^{13}C-depleted volcanic CO_2 emissions, likely from the Greater OJP or Southern KP, sustained the negative carbon isotope excursion during stage C3 (*5*, *22*). However, enrichment of Hg in Pacific Ocean water, recorded in DSDP Site 463 sediments, but not in Tethyan sediments cored at Cismon or Poggio Le Guaine, supports the hypothesis that OAE1a was driven by mantle-derived CO_2 emitted by Greater OJP volcanism rather than thermogenic methane release in the HALIP (*10*).

Our radioisotopic age model and chemostratigraphy for OAE1a in Japan can be compared to the chronology of OJP volcanism to gain insight into how these phenomena might be related. In our Bayesian age model (Fig. 2), segment C2 exhibits an excursion to unradiogenic Os_i (~0.34) at 119.668 +0.525/−0.064 Ma, followed by an excursion to even less radiogenic Os_i (~0.17) that began at 119.588 +0.047/−0.067 Ma and lasted 115 +57/−71 kyr. The latter excursion was followed at 119.549 +0.072/−0.079 Ma by an excursion to $\delta^{13}C_{org}$ of −28.75‰ that similarly lasted 115 +79/−75 kyr and that marks the onset of both segment C3 and OAE1a.

Although the chemostratigraphy from DSDP Site 463, Cismon, and Cau each display dual excursions toward unradiogenic Os_i that begin within segment C2, relative to the second Os_i excursion, the timing and magnitude of the negative $\delta^{13}C$ excursion at or near the base of segment C3 differ at each location. The age model from NKT constrains these three isotopic excursions to ~100 kyr, between ~119.67 and ~119.55 Ma, although the difference between the onset of the second Os_i excursion and the beginning of C3 is much

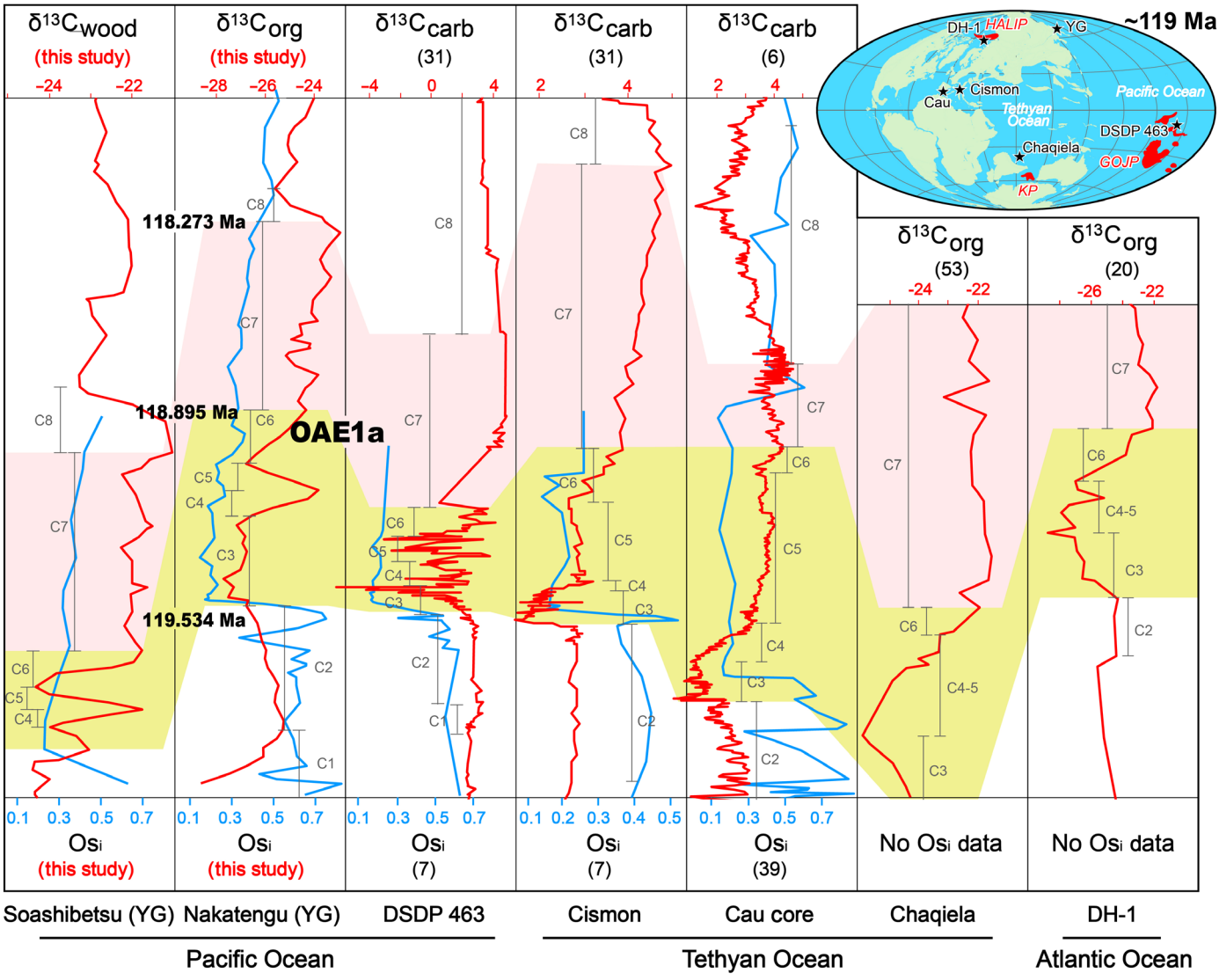

Fig. 3. Carbon and osmium chemostratigraphic correlation of NKT and SAB sections with widely distributed records. OAE1a is defined from segment C3 to C6 (yellow shaded region). We have interpreted the carbon isotope excursion segments from (*3*) in the Chaqiela (*53*) and DH-1 (*20*) records. HALIP, High Arctic Large Igneous Province; GOJP, Greater Ontong Java Plateau; KP, Kerguelen Plateau; YG, Yezo Group.

smaller (~39 kyr) (Fig. 2). The contrasting responses of seawater osmium and carbon at globally widespread localities (Fig. 3) may reflect differences in proximity to the mantle source of osmium and carbon and to sources of radiogenic continental sediment as well as deep ocean circulation pathways that operated during this brief period.

$^{40}Ar/^{39}Ar$ ages obtained from Greater OJP lavas in the 1990s (data S4) range from 127.3 to 122.3 Ma but with uncertainties of ±2 to 9 Ma (Fig. 4B). The NKT age model indicates that unradiogenic Os fluxed into the north Pacific Ocean at 119.67 Ma followed by an abrupt negative carbon isotope excursion and the onset of OAE1a at 119.55 Ma and is thus consistent with the flare-up of Greater OJP volcanism and transport of Os via intra-Pacific ocean currents prior to the C isotope excursion and the onset of ocean anoxia. $^{40}Ar/^{39}Ar$ ages obtained from Greater OJP lavas using modern analytical methods range from ~116 to 108 Ma and are used to argue that this volcanism is too young to be a driver for OAE1a (*18*). Although the recent $^{40}Ar/^{39}Ar$ ages are more precise than the legacy age determinations (Fig. 4B) (*18*), *L. cabri* forams are found in the oldest sediment overlying basaltic lavas from at least two of the cores (sites 1183 and 317) from which ages of 111.62 ± 0.55 and 116.53 ± 0.35 Ma were obtained for the OJP (*18*, *57*). If the NKT age model—based on U-Pb zircon dates—is accurate and *L. cabri* occurred prior to 118.4 Ma, then the chronostratigraphy of the Greater OJP and its sedimentary cover remains problematic with respect to its recent chronology (*18*). Thus, it is premature to rule out the OJP as a primary mechanistic driver of OAE1a.

A combination of an extremely high (nearly 40 cm/kyr) and constant rate of mudstone sedimentation, abundant rhyolitic tuffs containing datable zircon, and sufficient bulk organic matter for $\delta^{13}C_{org}$ and Re-Os analyses makes possible development of what may be the

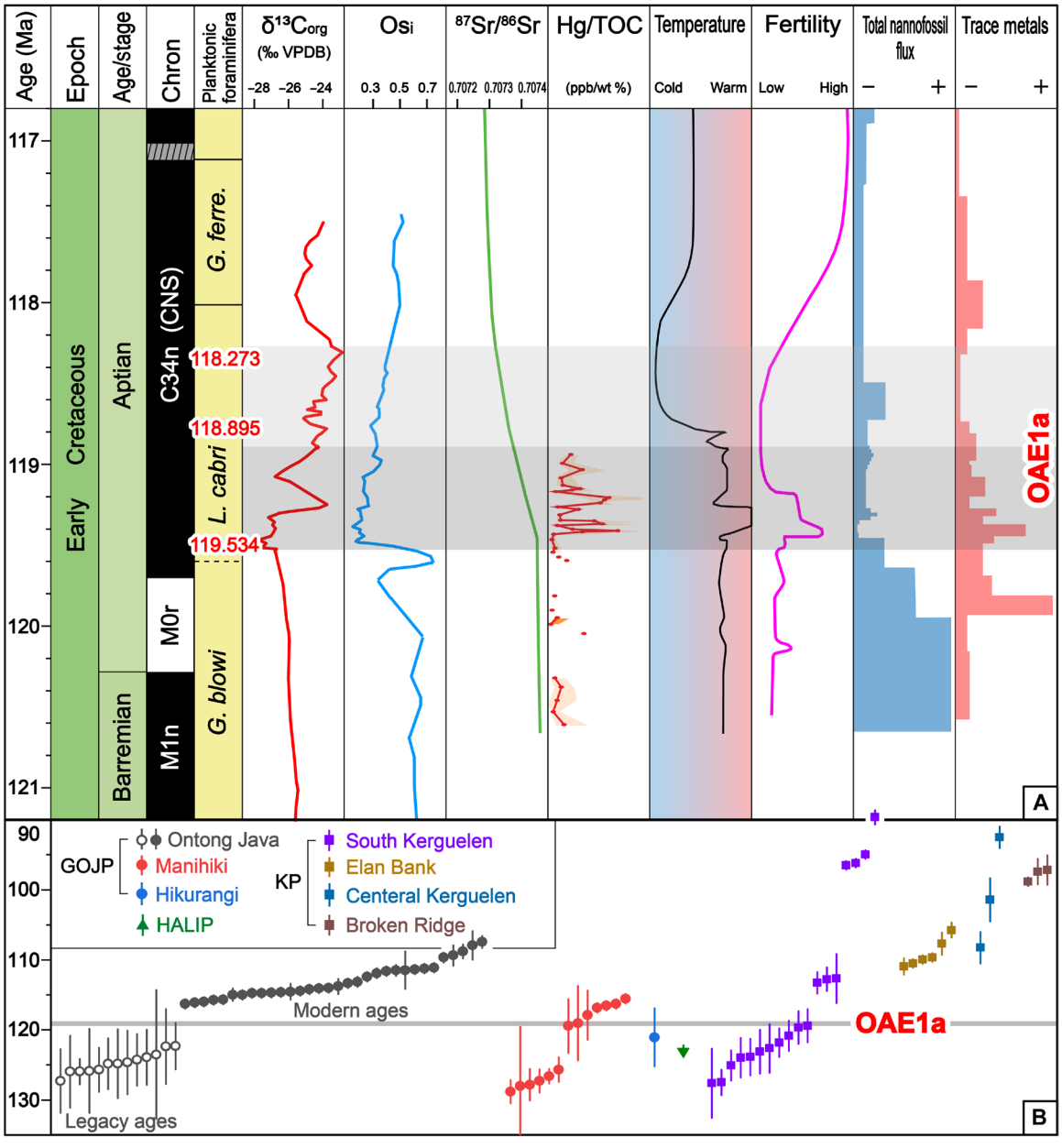

Fig. 4. Proposed age model for OAE1a. (**A**) Proposed age model for OAE1a and geochemical and paleobiologic proxies. Foraminifera zones from Geologic Time Scale 2020 (*48*, *49*). $\delta^{13}C_{org}$ and Os_i isotopic data are from the NKT section in this study. $^{87}Sr/^{86}Sr$ data from (*71*). Hg/TOC ratios for DSDP Site 463 from (*10*). Temperature is based on integrated oxygen isotopes (*5*, *71*, *72*). Fertility is from (*72*). Total nannofossil flux and trace metals are from (*5*). ppb, parts per billion. CNRS, Cretaceous Normal Superchron. (**B**) Age range of Greater OJP, HALIP, and KP. The $^{40}Ar/^{39}Ar$ and U-Pb ages are from sources in data S4. HALIP, High Arctic Large Igneous Province; GOJP, Greater Ontong Java Plateau; KP, Kerguelen Plateau; VPDB, Vienna Pee Dee belemnite; TOC, total organic carbon. From the Greater OJP, legacy $^{40}Ar/^{39}Ar$ ages in the 1990s are to the left, have large uncertainties (data S4), and are each older than 122 Ma, whereas modern ages from (*18*) to the right have much smaller uncertainties and are each younger than 116 Ma.

most highly resolved geochronologic and chronostratigraphic framework for any OAE interval yet to be investigated. Our results revise the Early Cretaceous timescale, bear directly on the question of volcanic initiation of OAE1a by OJP volcanism, provide impetus to reexamine the time series and spectral analyses that underpin astrochronologic age models, and will foster insights about Cretaceous paleoceanography as the Hokkaido age model is exported to other global sites.

MATERIALS AND METHODS

Carbon isotope analyses

Bulk mudstone samples (n = 64) from the SAB section were collected at 3- to 10-m stratigraphic intervals (Fig. 1C and data S2). Dry sample aliquots of 400 g were disaggregated using sodium tetraphenylborate plus sodium chloride. The disaggregated sediment was washed over a 64-μm sieve and dried at 50°C. Wood fragments (more than 100 fragments per sample) were picked up from

the processed samples and washed in methanol in an ultrasonic bath before immersion in 1 M HCl acid for 24 hours. The wood fragments were then dried and crushed to powder. The carbon isotope of the total organic carbon in the acid-treated powdered wood samples was then measured using a mass spectrometer (IsoPrime, GV Instruments) in line with an elemental analyzer (EuroEA3000, EuroVector) at the Tokyo University of Marine Science and Technology. Two specimens of each sample were measured, and carbon isotopic ratios are expressed as $\delta^{13}C_{wood}$ in ‰ units relative to the Vienna Pee Dee belemnite standard. The precision of the $\delta^{13}C$ measurements is ±0.1‰.

NKT section samples were crushed, weighed, and acidified at Northwestern University and analyzed at the Stable Isotope Core Laboratory at Washington State University (WSU) to determine the $\delta\ ^{13}C_{org}$ value of bulk organic matter. At WSU, samples were converted to CO_2 by combustion in an elemental analyzer (ECS 4010, Costech Analytical, Valencia, CA), separated with a 3-m gas chromatography column, and analyzed in a continuous flow isotope ratio mass spectrometer (DELTAplusXP, Thermo Finnigan, Bremen) (*58*, *59*). Isotopic reference materials were interspersed with samples for calibration. The 2 σ uncertainty of carbon isotopic results is 0.5‰ with duplicate samples measured at random through the section to confirm that measured values lie within the uncertainty bounds 95% of the time. Samples were normalized using two or more internal WSU running standards. Running standards were previously calibrated to NBS 18, NBS 19, RM 8542, and LSVEC as defined in the WSU Stable Isotope Core Laboratory library. The precision (1 σ) of standards used and associated normalization coefficients can be provided upon request.

Osmium isotope analyses

Determination of the water column osmium isotope ($^{187}Os/^{188}Os$) composition at the time of sediment deposition across the OAE1a interval was calculated from the rhenium-osmium (Re-Os) data of organic-bearing sedimentary units from the NKT (n = 68, from −273.5 to +253.2 m at ~10-m intervals) and SAB (n = 13, from 23.5 to 418.3 m) sections (Fig. 1C and data S3).

Every effort was made to collect fresh outcrop samples. Samples were further trimmed using a diamond saw blade with all surfaces polished to remove cutting and drilling marks to eliminate any potential contamination. The samples were dried at 60°C overnight and then were powdered in ceramic containers using high-purity crushing techniques at Northwestern University. The ceramic containers were cleaned using Ottawa sand, washed, and rinsed with ethanol. The powders were analyzed in the Durham Geochemistry Center at Durham University using ID negative ion mass spectrometry (*60*, *61*). In brief, sample powders (~1.0 g) were spiked with a mixed ^{185}Re + ^{190}Os tracer solution and digested in sealed Carius tubes with 8 ml of 0.25 g/g CrO_3 in 2 M H_2SO_4 for ~48 hours at 220°C, principally leaching hydrogenous Re and Os from organic matter. The Os fraction was isolated and purified via chloroform extraction with back reduction into HBr and CrO_3·H_2SO_4-HBr microdistillation. The Re fraction was isolated via NaOH-acetone extraction and anion chromatography. Isotopic ratios of samples and solution standards (Re STD [rhenium standard solution] and DROsS [Durham Romil Osmium Standard solution]) were measured on a Thermo Fisher Scientific Triton thermal ionization mass spectrometer in negative ionization mode. Running average values for $^{187}Os/^{188}Os$ and $^{185}Re/^{187}Re$ solution standards to the time of these analyses (September 2023) were 0.16083 ± 0.00058 (1 σ SD, n = 980) and 0.59861 ± 0.00143 (1 σ SD, n = 819), respectively. Total procedural blanks during this study were 11.3 ± 2.8 and 0.05 ± 0.02 pg (1 σ SD, N = 13) for Re and Os, respectively, with an average $^{187}Os/^{188}Os$ value of 0.21 ± 0.03 (N = 13). Present-day measured $^{187}Os/^{188}Os$ values of samples were corrected to initial $^{187}Os/^{188}Os$ values (Os_i) by accounting for postdepositional beta decay of ^{187}Re [$\lambda = 1.666 \times 10^{-11}$ $year^{-1}$ (*62*)] using an age of 119.0 Ma.

U-Pb dating and Bayesian age-depth modeling

A total of 6 tuffs in the SAB section and 13 in the NKT section were collected for U-Pb zircon CA-ID-TIMS dating (Fig. 1, B and C, and figs. S1 and S2) at the Boise State University Isotope Geology Laboratory. Zircon crystals were placed in muffle furnaces at 900°C for 60 hours to anneal radiation-damaged domains (*63*). Individual crystals were mounted in epoxy, polished to center zones, and imaged by cathodoluminescence (CL). From the compiled images, spots were selected for laser ablation–inductively coupled plasma mass spectrometry (LA-ICPMS) using a Teledyne Photon Machines Analyte Excite+ 193-nm excimer laser and Thermo Scientific iCap RQ quadrupole ICPMS. On the basis of CL images and LA-ICPMS data, single zircon grains were plucked from their respective epoxy mounts for the subsequent CA-ID-TIMS analysis. Individual zircon grains were chemically abraded in concentrated (29 M) HF at 190°C for 12 hours to mitigate open-system behavior and remove inclusions (*63*). The residual zircon grains were spiked with the EARTHTIME mixed ET535 or ET2535 tracer solution (*64*, *65*) and completely dissolved in 29 M HF at 220°C for 48 hours in Parr bombs. Following dissolution, the zircon+tracer solutions were dried to fluorides and then redissolved in 6 M HCl at 180°C overnight. Uranium and Pb were separated by anion-exchange column chromatography using 50-μl columns and AG-1 X8 resin (*66*). The U and Pb isotopic measurements were performed on an IsotopX Phoenix X62 multicollector thermal ionization mass spectrometer. Determined U-Pb dates and uncertainties for each analysis were calculated from isotope ratio measurements using the algorithms of (*67*) and the U decay constants of (*68*).

Bayesian age-depth modeling uses the open-source R package modified BChron (*47*, *69*), which is an adaptation of Bchron (*70*) for use in deeper time geologic settings. The models were evaluated at a resolution of 1 m, recovering the median and 95% highest density interval (HDI) of the posterior distribution of age for every stratigraphic position from 20,000 accepted iterations (after a burn-in of 1000) of the Markov chain Monte Carlo random walks using an adaptive Metropolis-Hastings proposal. Ages and uncertainties for key horizons and intervals were evaluated from the 95% credible interval of the posterior distribution. Obtaining the interval durations required a simple postmodeling step: Temporal durations were extracted from the model output by calculating the difference between two distinct horizons for all Markov chain iterations, and the duration and uncertainty were determined from the 2.5, 50, and 97.5% quantiles (95% credible interval) of the extracted differences. Model results incorporate only the analytical uncertainties from weighted mean or Bayesian ages. When comparing our model results to those developed with data from a different radioisotope decay scheme, a systematic uncertainty of 0.11% representing U-Pb tracer and ^{238}U decay constant uncertainties must be propagated on all posterior ages and durations.

Supplementary Materials

The PDF file includes:

Supplementary Text
Figs. S1 to S7
Table S1
Legends for data S1 to S4
References

Other Supplementary Material for this manuscript includes the following:

Data S1 to S4

REFERENCES AND NOTES

1. S. O. Schlanger, H. C. Jenkyns, Cretaceous oceanic anoxic events: Causes and consequences. *Geol. Mijnb.* **55**, 179–184 (1976).
2. M. A. Arthur, H. C. Jenkyns, H. Brumsack, S. O. Schlanger, "Stratigraphy, geochemistry, and paleoceanography of organic carbon-rich Cretaceous sequences" in *Cretaceous Resources, Events and Rhythms: Background and Plans for Research*, R. N. Ginsburg, B. Beaudoin, Eds., NATO ASI Series (Springer, 1990), vol. 304, pp. 75–119.
3. A. P. Menegatti, H. Weissert, R. S. Brown, R. V. Tyson, P. Farrimond, A. Strasser, M. Caron, High-resolution $\delta^{13}C$ stratigraphy through the early Aptian "Livello Selli" of the Alpine Tethys. *Paleoceanography* **13**, 530–545 (1998).
4. H. C. Jenkyns, Geochemistry of oceanic anoxic events. *Geochem. Geophys. Geosys.* **11**, Q03004 (2010).
5. E. Erba, R. A. Duncan, C. Bottini, D. Tiraboschi, H. Weissert, H. C. Jenkyns, A. Malinverno, in *Environmental Consequences of Ontong Java Plateau and Kerguelen Plateau volcanism*, Geological Society of America Special Paper, **511**, 271–303 (2015).
6. J. M. Castro, P. A. Ruiz-Ortiz, G. A. de Gea, R. Aguado, I. Jarvis, H. Weissert, J. M. Molina, L. M. Nieto, R. D. Pancost, M. L. Quijano, M. Reolid, High-resolution C-isotope, TOC and biostratigraphic records of OAE 1a (Aptian) from an expanded hemipelagic cored succession, western Tethys: A new stratigraphic reference for global correlation and paleoenvironmental reconstruction. *Paleoceanogr. Paleoclimatol.* **36**, e2020PA004004 (2021).
7. C. Bottini, A. S. Cohen, E. Erba, H. C. Jenkyns, A. L. Coe, Osmium isotope evidence for volcanism, weathering and ocean mixing during the early Aptian OAE 1a. *Geology* **40**, 583–586 (2012).
8. B. D. A. Naafs, R. D. Pancost, Sea-surface temperature evolution across Aptian Oceanic Anoxic event 1a. *Geology* **44**, 959–962 (2016).
9. H. C. Jenkyns, Transient cooling episodes during Cretaceous Oceanic Anoxic events with special reference to OAE 1a (Early Aptian). *Philos. Trans. A Math. Phys. Eng. Sci.* **376**, 20170073 (2018).
10. L. M. E. Percival, L. R. Tedeschi, R. A. Creaser, C. Bottini, E. Erba, F. Giraud, H. Svensen, J. Savian, R. Trindade, R. Coccioni, F. Frontalini, Determining the style and provenance of magmatic activity during the early Aptian Oceanic Anoxic event (OAE 1a). *Glob. Planet. Change* **200**, 103461 (2021).
11. J. Wang, A. D. Jacobson, B. B. Sageman, M. T. Hurtgen, Stable Ca and Sr isotopes support volcanically triggered biocalcification crisis during Oceanic Anoxic event 1a. *Geology* **49**, 515–519 (2021).
12. H. Weissert, J. A. McKenzie, J. E. T. Channell, "Natural variations in the carbon cycle during the Early Cretaceous" in *The Carbon Cycle and Atmospheric CO_2: Natural Variations Archean to Present*, E. Sundquist, W. E. Broecker, Eds., Geophysical Monograph Series (American Geophysical Union, 1985), vol. 32, pp. 531–545.
13. R. Coccioni, R. Franchi, O. Nesci, C. F. Wezel, F. Battistini, P. Pallecchi, Stratigraphy and mineralogy of the Selli level (early Aptian) at the base of the Marne a Fucoidi in the Umbrian-Marche Apennines (Italy), in *Cretaceous of the Western Tethys: Proceedings of the 3rd International Cretaceous Symposium*, J. Weidmann, Ed. (Schweizerbart, 1989), pp. 563–584.
14. E. Erba, J. E. T. Channell, M. Claps, C. Jones, R. Larson, B. Opdyke, I. P. Silva, A. Riva, G. Salvini, S. Torricelli, Integrated Stratigraphy of the Cismon APTICORE (Southern Alps, Italy): A "reference section" for the Barremian–Aptian interval at low latitudes. *J. Foraminiferal Res.* **29**, 371–391 (1999).
15. M. L. G. Tejada, K. Suzuki, J. Kuroda, R. Coccioni, J. J. Mahoney, N. Ohkouchi, T. Sakamoto, Y. Tatsumi, Ontong Java Plateau eruption as a trigger for the early Aptian oceanic anoxic event. *Geology* **37**, 855–858 (2009).
16. S. Méhay, C. E. Keller, S. M. Bernasconi, H. Weissert, E. Erba, C. Bottini, P. A. Hochuli, A volcanic CO_2 pulse triggered the Cretaceous Oceanic Anoxic Event 1a and a biocalcification crisis. *Geology* **37**, 819–822 (2009).
17. G. Charbonnier, K. B. Föllmi, Mercury enrichments in lower Aptian sediments support the link between Ontong Java large igneous province activity and oceanic anoxic episode 1a. *Geology* **45**, 63–66 (2017).
18. P. C. Davidson, A. A. P. Koppers, T. Sano, T. Hanyu, A younger and protracted emplacement of the Ontong Java Plateau. *Science* **380**, 1185–1188 (2023).
19. S. Polteau, B. W. Hendriks, S. Planke, M. Ganerød, F. Corfu, J. I. Faleide, I. Midtkandal, H. S. Svensen, R. Myklebust, The Early Cretaceous Barents Sea Sill Complex: Distribution, $^{40}Ar/^{39}Ar$ geochronology, and implications for carbon gas formation. *Palaeogeogr. Palaeoclimatol. Palaeoecol.* **441**, 83–95 (2016).
20. I. Midtkandal, H. H. Svensen, S. Planke, F. Corfu, S. Polteau, T. H. Torsvik, J. I. Faleide, S. A. Grundvåg, H. Selnes, W. Kürschner, S. Olaussen, The Aptian (Early Cretaceous) oceanic anoxic event (OAE1a) in Svalbard, Barents Sea, and the absolute age of the Barremian-Aptian boundary. *Palaeogeogr. Palaeoclimatol. Palaeoecol.* **463**, 126–135 (2016).
21. M. Adloff, S. E. Greene, I. J. Parkinson, B. D. A. Naafs, W. Preston, A. Ridgwell, D. J. Lunt, J. M. C. Jiménez, F. M. Monteiro, Unravelling the sources of carbon emissions at the onset of oceanic anoxic event (OAE) 1a. *Earth Planet. Sci. Lett.* **530**, 115947 (2020).
22. Q. Jiang, F. Jourdan, H. K. Olierook, R. E. Merle, J. Bourdet, D. Fougerouse, B. Godel, A. T. Walker, Volume and rate of volcanic CO_2 emissions governed the severity of past environmental crises. *Proc. Natl. Acad. Sci. U.S.A.* **119**, e2202039119 (2022).
23. Y. X. Li, T. J. Bralower, I. P. Montañez, D. A. Osleger, M. A. Arthur, D. M. Bice, T. D. Herbert, E. Erba, I. P. Silva, Toward an orbital chronology for the early Aptian Oceanic Anoxic event (OAE1a, ~120 Ma). *Earth Planet. Sci. Lett.* **271**, 88–100 (2008).
24. A. Malinverno, E. Erba, T. D. Herbert, Orbital tuning as an inverse problem: Chronology of the early Aptian oceanic anoxic event 1a (Selli level) in the Cismon APTICORE. *Paleoceanography* **25**, PA2203 (2010).
25. C. J. Huang, L. A. Hinnov, A. G. Fischer, A. Grippo, T. Herbert, Astronomical tuning of the Aptian Stage from Italian reference sections. *Geology* **38**, 899–902 (2010).
26. Y. Zhang, J. G. Ogg, D. Minguez, M. W. Hounslow, S. Olaussen, F. M. Gradstein, S. Esmeray-Senlet, Magnetostratigraphy of U-Pb–dated boreholes in Svalbard, Norway, implies that magnetochron M0r (a proposed Barremian-Aptian boundary marker) begins at 121.2 ± 0.4 Ma. *Geology* **49**, 733–737 (2021).
27. C. G. Leandro, J. F. Savian, M. V. L. Kochhann, D. R. Franco, R. Coccioni, F. Frontalini, S. Gardin, L. Jovane, M. Figueiredo, L. R. Tedeschi, L. Janikian, Astronomical tuning of the Aptian Stage and its implications for age recalibrations and paleoclimatic events. *Nat. Commun.* **13**, 2941 (2022).
28. Y. J. Li, H. F. Qin, B. R. Jicha, M. H. Huyskens, C. J. Wall, R. B. Trayler, Q. Z. Yin, M. Schmitz, Y. X. Pan, C. L. Deng, B. S. Singer, H. Y. He, R. X. Zhu, Revised onset age of magnetochron M0r: Chronostratigraphic and geologic implications. *Geology* **51**, 565–570 (2023).
29. M. Moullade, G. Tronchetti, B. Granier, A. Bornemann, W. Kuhnt, J. Lorenzen, High-resolution integrated stratigraphy of the OAE1a and enclosing strata from core drillings in the Bedoulian stratotype (Roquefort-La Bédoule, SE France). *Cretac. Res.* **56**, 119–140 (2015).
30. A. Ando, T. Kakegawa, R. Takashima, T. Saito, New perspective on Aptian carbon isotope stratigraphy: Data from $\delta^{13}C$ records of terrestrial organic matter. *Geology* **30**, 227–230 (2002).
31. C. Bottini, E. Erba, D. Tiraboschi, H. C. Jenkyns, S. Schouten, J. S. Sinninghe Damsté, Climate variability and ocean fertility during the Aptian Stage. *Clim. Past* **11**, 383–402 (2015).
32. R. Takashima, F. Kawabe, H. Nishi, K. Moriya, R. Wani, H. Ando, Geology and stratigraphy of forearc basin sediments in Hokkaido, Japan: Cretaceous environmental events on the north-west Pacific margin. *Cretac. Res.* **25**, 365–390 (2004).
33. T. Saito, A. Ando, New findings of the planktonic foraminifer *Leupoldina cabri* (Sigal, 1952) from the Sorachi Group of Hokkaido, Japan and its bearing on the Cretaceous chronology of northwestern Pacific marine strata. *Bull. Natn. Sci. Mus. Tokyo, Ser. C* **26**, 183–191 (2000).
34. H. Nishi, R. Takashima, T. Hatsugai, T. Saito, K. Moriya, A. Ennyu, T. Sakai, Planktonic foraminiferal zonation in the Cretaceous Yezo Group, Central Hokkaido, Japan. *J. Asian Earth Sci.* **21**, 867–886 (2003).
35. H. Koyasu, H. Nishi, R. Takashima, N. Suzuki, Cretaceous radiolarian biostratigraphy in the Yezo group, Hokkaido, Northeast Japan. *Newsl. Stratigr.* **52**, 297–319 (2019).
36. I. P. Silva, W. V. Sliter, "Cretaceous paleoceanography: Evidence from planktonic foraminiferal evolution" in *Evolution of the Cretaceous Ocean-Climate System*, E. Barrera, C. C. Johnson, Eds., Geological Society of America Special Paper **332**, 301–328 (1999).
37. I. P. Silva, E. Erba, G. Salvini, C. Locatelli, D. Verga, Biotic changes in Cretaceous oceanic anoxic events of the Tethys. *J. Foraminiferal Res.* **29**, 352–370 (1999).
38. R. Talbi, A. Amri, A. Boujemaa, H. Gabtni, R. Spiller, R. Levey, First evidence of the early Cretaceous oceanic anoxic events (MBE and OAE1a) in the southern Tethyan margin (NE-Tunisia): Biostratigraphy and shale resource system. *J. Petrol. Explor. Prod. Technol.* **11**, 1559–1575 (2021).
39. R. Martínez-Rodríguez, D. Selby, J. M. Castro, G. A. de Gea, L. M. Nieto, P. A. Ruiz-Ortiz, Tracking magmatism and oceanic change through the early Aptian Anoxic Event (OAE 1a) to the late Aptian: Insights from osmium isotopes from the westernmost Tethys (SE Spain) Cau Core. *Glob. Planet. Change* **207**, 103652 (2021).
40. A. Ando, T. Kakegawa, R. Takashima, T. Saito, Stratigraphic carbon isotope fluctuations of detrital woody materials during the Aptian Stage in Hokkaido, Japan: Comprehensive $\delta^{13}C$ data from four sections of the Ashibetsu area. *J. Asian Earth Sci.* **21**, 835–847 (2003).

41. J. Socorro, F. J.-M. R. Maurrasse, Continuous accumulation of organic matter-rich sediments associated with Oceanic Anoxic Event 1a in the El Pujal section, Organya Basin, Catalunya, Spain and its relation to episodic dysoxia. *Cretac. Res.* **95**, 225–251 (2019).
42. H. Matsumoto, M. L. G. Tejada, K. T. Goto, G. Shimoda, Y. Watanabe, K. Shirai, A. Ishikawa, A. Ando, T. Sano, J. Kuroda, K. Suzuki, Brief and intensive volcanic emissions from Ontong Java Nui heralded Oceanic Anoxic Event 1a. *Commun. Earth Environ.* **5**, 155 (2024).
43. H. C. Jenkyns, Carbon-isotope stratigraphy and paleoceanographic significance of the Lower Cretaceous shallow-water carbonates of Resolution Guyot, Mid-Pacific Mountains, in *Proceedings of the Ocean Drilling Program: Scientific Results*, E. L. Winterer, W. W. Sager, J. V. Firth, J. M. Sinton, Eds. (Ocean Drilling Program, 1995), vol. 143, pp. 99–104.
44. W. R. Thompson, On a criterion for the rejection of observations and the distribution of the ratio of deviation to sample standard deviation. *Ann. Math. Statist.* **6**, 214–219 (1935).
45. C. B. Keller, B. Schoene, K. M. Samperton, A stochastic sampling approach to zircon eruption age interpretation. *Geochem. Perspect. Lett.* **8**, 31–35 (2018).
46. D. Condon, B. Schoene, M. Schmitz, U. Schaltegger, R. B. Ickert, Y. Amelin, L. E. Augland, K. R. Chamberlain, D. S. Coleman, J. N. Connelly, F. Corfu, J. L. Crowley, J. H. F. L. Davies, S. W. Denyszyn, M. P. Eddy, S. P. Gaynor, L. M. Heaman, M. H. Huyskens, S. Kamo, J. Kasbohm, C. B. Keller, S. A. Mac Lennan, N. M. Mc Lean, S. Noble, M. Ovtcharova, A. Paul, J. Ramezani, M. Rioux, D. Sahy, J. S. Scoates, D. Szymanowski, S. Tapster, M. Tichomirowa, C. J. Wall, J.-F. Wotzlaw, C. Yang, Q.-Z. Yin, Recommendations for the reporting and interpretation of isotope dilution U-Pb geochronological information. *Geol. Soc. Am. Bull.* **136**, 4233–4251 (2024).
47. R. B. Trayler, M. D. Schmitz, J. I. Cuitiño, M. J. Kohn, M. S. Bargo, R. F. Kay, C. A. E. Strömberg, S. F. Vizcaíno, An improved approach to age-modeling in deep time: Implications for the Santa Cruz Formation, Argentina. *Geol. Soc. Am. Bull.* **132**, 233–244 (2020).
48. A. S. Gale, J. Mutterlose, S. Batenburg, "The Cretaceous Period" in *The Geologic Time Scale 2020, Volume 2*, F. M. Gradstein, J. G. Ogg, M. D. Schmitz, G. M. Ogg, Eds. (Elsevier, 2020), pp. 1023–1086.
49. J. G. Ogg, "Geomagnetic polarity time scale" in *The Geologic Time Scale 2020, Volume 1*, F. M. Gradstein, J. G. Ogg, M. D. Schmitz, G. M. Ogg, Eds. (Elsevier, 2020), pp. 159–192.
50. E. C. van Bentum, G. J. Reichart, A. Forster, J. S. Sinninghe Damsté, Latitudinal differences in the amplitude of the OAE-2 carbon isotopic excursion: pCO_2 and paleo productivity. *Biogeosciences* **9**, 717–731 (2012).
51. I. Wendler, A critical evaluation of carbon isotope stratigraphy and biostratigraphic implications for Late Cretaceous global correlation. *Earth Sci. Rev.* **126**, 116–146 (2013).
52. A. Ando, K. Kaiho, H. Kawahata, T. Kakegawa, Timing and magnitude of early Aptian extreme warming: Unraveling primary $\delta^{18}O$ variation in indurated pelagic carbonates at Deep Sea Drilling Project Site 463, central Pacific Ocean. *Palaeogeogr. Palaeoclimatol. Palaeoecol.* **260**, 463–476 (2008).
53. X. L. Zhang, K. F. Chen, D. P. Hu, J. G. Sha, Mid-Cretaceous carbon cycle perturbations and Oceanic Anoxic Events recorded in southern Tibet. *Sci. Rep.* **6**, 39643 (2016).
54. K. Misumi, Y. Yamanaka, E. Tajika, Numerical simulation of atmospheric and oceanic biogeochemical cycles to an episodic CO_2 release event: Implications for the cause of mid-Cretaceous Ocean Anoxic Event-1a. *Earth Planet. Sci. Lett.* **286**, 316–323 (2009).
55. A. H. Jahren, C. P. Conrad, N. C. Arens, G. Mora, C. Lithgow-Bertelloni, A plate tectonic mechanism for methane hydrate release along subduction zones. *Earth Planet. Sci. Lett.* **236**, 691–704 (2005).
56. H. Matsumoto, R. Coccioni, F. Frontalini, K. Shirai, L. Jovane, R. Trindade, J. F. Savian, M. L. G. Tejada, S. Gardin, J. Kuroda, Long-term Aptian marine osmium isotopic record of Ontong Java Nui activity. *Geology* **49**, 1148–1152 (2021).
57. P. J. Sikora, J. A. Bergen, "Lower Cretaceous planktonic foraminiferal and nannofossil biostratigraphy of Ontong Java Plateau sites from DSDP Leg 30 and ODP Leg 192" in *Origin and Evolution of the Ontong Java Plateau*, J. G. Fitton, J. J. Mahoney, P. J. Wallace, A. D. Saunders, Eds., Geological Society, London, Special Publications **229,** 83–111 (2004).
58. J. T. Brenna, T. N. Corso, H. J. Tobias, R. J. Caimi, High-precision continuous-flow isotope ratio mass spectrometry. *Mass Spectrom. Rev.* **16**, 227–258 (1997).
59. H. Qi, T. B. Coplen, H. Geilmann, W. A. Brand, J. K. Böhlke, Two new organic reference materials for $\delta^{13}C$ and $\delta^{15}N$ measurements and a new value for the $\delta^{13}C$ of NBS 22 oil. *Rapid Commun. Mass Spectrom.* **17**, 2483–2487 (2003).
60. D. Selby, R. A. Creaser, Re-Os geochronology of organic rich sediments: An evaluation of organic matter analysis methods. *Chem. Geol.* **200**, 225–240 (2003).
61. V. M. Cumming, S. W. Poulton, A. D. Rooney, D. Selby, Anoxia in the terrestrial environment during the late Mesoproterozoic. *Geology* **41**, 583–586 (2013).
62. M. I. Smoliar, R. J. Walker, J. W. Morgan, Re-Os ages of group IIA, IIIA, IVA, and IVB iron meteorites. *Science* **271**, 1099–1102 (1996).
63. J. M. Mattinson, Zircon U–Pb chemical abrasion ("CA-TIMS") method: Combined annealing and multi-step partial dissolution analysis for improved precision and accuracy of zircon ages. *Chem. Geol.* **220**, 47–66 (2005).
64. D. J. Condon, B. Schoene, N. M. McLean, S. A. Bowring, R. R. Parrish, Metrology and traceability of U–Pb isotope dilution geochronology (EARTHTIME Tracer Calibration Part I). *Geochim. Cosmochim. Acta* **164**, 464–480 (2015).
65. N. M. McLean, D. J. Condon, B. Schoene, S. A. Bowring, Evaluating uncertainties in the calibration of isotopic reference materials and multi-element isotopic tracers (EARTHTIME Tracer Calibration Part II). *Geochim. Cosmochim. Acta* **164**, 481–501 (2015).
66. T. E. Krogh, A low-contamination method for hydrothermal decomposition of zircon and extraction of U and Pb for isotopic age determinations. *Geochim. Cosmochim. Acta* **37**, 485–494 (1973).
67. M. D. Schmitz, B. Schoene, Derivation of isotope ratios, errors and error correlations for U-Pb geochronology using ^{205}Pb-^{235}U-(^{233}U)-spiked isotope dilution thermal ionization mass spectrometric data. *Geochem. Geophys. Geosyst.* **8**, Q08006 (2007).
68. A. Jaffey, K. Flynn, L. Glendenin, W. T. Bentley, A. Essling, Precision measurement of half-lives and specific activities of ^{235}U and ^{238}U. *Phys. Rev. C* **4**, 1889–1906 (1971).
69. R Core Team, *R: A Language and Environment for Statistical Computing* (R Foundation for Statistical Computing, 2023).
70. A. C. Parnell, J. Haslett, J. R. Allen, C. E. Buck, B. Huntley, A flexible approach to assessing synchroneity of past events using Bayesian reconstructions of sedimentation history. *Quat. Sci. Rev.* **27**, 1872–1885 (2008).
71. H. Weissert, E. Erba, Volcanism, CO_2 and palaeoclimate: A Late Jurassic–Early Cretaceous carbon and oxygen isotope record. *J. Geol. Soc. London* **161**, 695–702 (2004).
72. E. Erba, C. Bottini, H. J. Weissert, C. E. Keller, Calcareous nannoplankton response to surface-water acidification around Oceanic Anoxic Event 1a. *Science* **329**, 428–432 (2010).
73. J. Lorenzen, W. Kuhnt, A. Holbourn, S. Flögel, M. Moullade, G. Tronchetti, A new sediment core from the Bedoulian (lower Aptian) stratotype at Roquefort–La Bédoule, SE France. *Cretac. Res.* **39**, 6–16 (2013).
74. J. O. Herrle, P. Kößler, O. Friedrich, H. Erlenkeuser, C. Hemleben, High-resolution carbon isotope records of the Aptian to Lower Albian from SE France and the Mazagan Plateau (DSDP site 545): A stratigraphic tool for paleoceanographic and paleobiologic reconstruction. *Earth Planet. Sci. Lett.* **218**, 149–161 (2004).
75. T. J. Bralower, E. CoBabe, B. Clement, W. V. Sliter, C. L. Osburn, J. F. Longoria, The record of global change in mid-Cretaceous (Barremian–Albian) sections from the Sierra Madre, northeastern Mexico. *J. Foraminiferal Res.* **29**, 418–437 (1999).
76. P. A. Fernandez-Mendiola, J. Mendicoa, H. G. Owen, J. García-Mondéjar, The early Aptian (Cretaceous) stratigraphy of Mount Pagasarri (N Spain): Oceanic anoxic event-1a. *Geol. J.* **53**, 1802–1822 (2018).
77. J. Hiess, D. J. Condon, N. McLean, S. R. Noble, $^{238}U/^{235}U$ systematics in terrestrial uranium-bearing minerals. *Science* **335**, 1610–1614 (2012).
78. I. Wendt, C. Carl, The statistical distribution of the mean squared weighted deviation. *Chem. Geol. Isot. Geosci.* **86**, 275–285 (1991).
79. J. J. Mahoney, M. Storey, R. A. Duncan, K. J. Spencer, M. Pringle, "Geochemistry and Age of the Ontong Java Plateau" in *The Mesozoic Pacific: Geology, Tectonics, and Volcanism*, Geophysical Monograph Series (American Geophysical Union, 1993), vol. 77, pp. 233–261.
80. L. M. Chambers, M. S. Pringle, J. G. Fitton, Phreatomagmatic eruptions on the Ontong Java Plateau: An Aptian $^{40}Ar/^{39}Ar$ age for volcaniclastic rocks at ODP Site 1184. *Geol. Soc. Spec. Publ.* **229**, 325–331 (2004).
81. M. L. G. Tejada, J. J. Mahoney, R. A. Duncan, M. P. Hawkins, Age and geochemistry of basement and alkalic rocks of Malaita and Santa Isabel, Solomon Islands, southern margin of Ontong Java Plateau. *J. Petrol.* **37**, 361–394 (1996).
82. K. Hoernle, F. Hauff, P. Van den Bogaard, R. Werner, N. Mortimer, J. Geldmacher, D. Garbe-Schönberg, B. Davy, Age and geochemistry of volcanic rocks from the Hikurangi and Manihiki oceanic Plateaus. *Geochim. Cosmochim. Acta* **74**, 7196–7219 (2010).
83. C. Timm, K. Hoernle, R. Werner, F. Hauff, P. van den Bogaard, P. Michael, M. F. Coffin, A. Koppers, Age and geochemistry of the oceanic Manihiki Plateau, SW Pacific: New evidence for a plume origin. *Earth Planet. Sci. Lett.* **304**, 135–146 (2011).
84. S. Ingle, J. J. Mahoney, H. Sato, M. F. Coffin, J. I. Kimura, N. Hirano, M. Nakanishi, Depleted mantle wedge and sediment fingerprint in unusual basalts from the Manihiki Plateau, central Pacific Ocean. *Geology* **35**, 595–598 (2007).
85. M. L. G. Tejada, T. Sano, T. Hanyu, A. A. P. Koppers, M. Nakanishi, T. Miyazaki, A. Ishikawa, K. Tani, S. Shimizu, K. Shimizu, B. Vaglarov, New evidence for the Ontong Java Nui hypothesis. *Sci. Rep.* **13**, 8486 (2023).
86. Q. Jiang, F. Jourdan, H. K. Olierook, R. E. Merle, J. M. Whittaker, Longest continuously erupting large igneous province driven by plume-ridge interaction. *Geology* **49**, 206–210 (2021).
87. M. F. Coffin, M. S. Pringle, R. A. Duncan, T. P. Gladczenko, M. Storey, R. D. Müller, L. A. Gahagan, Kerguelen hotspot magma output since 130 Ma. *J. Petrol.* **43**, 1121–1137 (2002).
88. R. A. Duncan, A time frame for construction of the Kerguelen Plateau and Broken Ridge. *J. Petrol.* **43**, 1109–1119 (2002).
89. K. Min, R. Mundil, P. R. Renne, K. R. Ludwig, A test for systematic errors in $^{40}Ar/^{39}Ar$ geochronology through comparison with U/Pb analysis of a: 1.1-Ga rhyolite. *Geochim. Cosmochim. Acta* **64**, 73–98 (2000).
90. K. F. Kuiper, A. Deino, F. J. Hilgen, W. Krijgsman, P. R. Renne, J. R. Wijbrans, Synchronizing rock clocks of Earth history. *Science* **320**, 500–504 (2008).

Acknowledgments: We thank J. Crowley for assistance with U-Pb analytical work and B. Wathen and A. Baudry for extraction of zircon from tuffs. A. Masterson made important contributions to the early phase of carbon isotope analysis. We also acknowledge M. Lott at Washington State University's Stable Isotope Core Lab for the C isotope measurements. S. Kuwabara, T. Kitami, and S. Tanaka made contribution to the field collection of samples. C. Ottley and G. Nowell are acknowledged for laboratory support. **Funding:** This work was supported by US NSF grants EAR-1951812 (B.S.S.), EAR-1952346 (M.D.S.), and EAR-1951835 (B.B.S.); UK NERC grant NE/V019406/1 (D.S.); and Japan Science Foundation grants KAKENHI 21H04503 and 18KK0091 (R.T.). **Author contributions:** Conceptualization: B.S.S., R.T., M.D.S., B.B.S., and D.S. Methodology: Y.L., M.D.S., L.G.P., D.S., T.Y., M.T.M., and K.S. Investigation: B.S.S., R.T., K.H., T.T., L.G.P., T.Y., B.B.S., and K.S. Visualization: Y.L. Funding acquisition: B.S.S., R.T., M.D.S., B.B.S., and D.S. Project administration: B.S.S., R.T., M.D.S., B.B.S., and D.S. Supervision: B.S.S., R.T., M.D.S., B.B.S., and D.S. Writing—original draft: Y.L. Writing—review and editing: Y.L., B.S.S., B.B.S., M.D.S., D.S., L.G.P., R.T., and M.T.M. **Competing interests:** The authors declare that they have no competing interests. **Data and materials availability:** All data needed to evaluate the conclusions in the paper are present in the paper and/or the Supplementary Materials.

Submitted 2 January 2024
Accepted 16 October 2024
Published 20 November 2024
10.1126/sciadv.adn8365